Supplementary of

Numerical modeling on the mechanisms of chlorine chemistry in snowpack and their impact on secondary atmospheric pollution

Shengjin Xie et al.

Correspondence to: Xuelei Zhang (zhangxuelei@iga.ac.cn)

This supplementary document consists of including 2 text, 6 Figures and 3 Tables.

Text captions

Text S1. N_2O_5 uptake and $ClNO_2$ production on snowpack.

Text S2. Snow parameters observed by satellite remote sensing.

Figure captions

Figure S1. Characterization of S/V_g under different LU-LC.

Figure S2. N_2O_5 uptake and $ClNO_2$ yield on the ground surfaces (snow, vegetation, and buildings).

Figure S3. Comparison between simulated and observed concentrations of N_2O_5 and $ClNO_2$ under the BT09 and YU20 schemes.

Figure S4. Monthly average spatial distribution of snow parameters (snow depth, snow cover, snow albedo and snow density).

Figure S5. Spatial distribution of oxidative species (OH, HO_2, RO_2) in different scenarios.

Figure S6. The quantitative contribution of different pathways of chlorine chemistry on atmospheric oxidizing capacity. The three columns of panels represent the changes in concentrations of OH (left), RO_2 (middle), and HO_2 (right) radicals, respectively. (a–f) The bottom two rows in each group show the corresponding relative changes (%).

Figure S7. Spatial distribution of $PM_{2.5}$ and its component species in different scenarios.

Figure S8. The contribution of the photolysis process of $ClNO_2$ on the ground surface.

Table captions

Table S1. Chlorine emissions from the ACEIC and MEIC anthropogenic inventories used in this study (unit: Gg).

Table S2. Model configurations of WRF and CAMx.

Table S3. Heterogeneous chemical reaction parameter schemes of N_2O_5 on aerosol surface.

Table S4. Comparative analysis of statistical indicators for the simulation results of N_2O_5 heterogeneous processes on atmospheric aerosol surfaces under different parameter schemes.

Text captions

Text S1. N_2O_5 uptake and $ClNO_2$ Production on snowpack:

Previous studies in mid-latitude regions report a snow particle radius (r_s) near the surface ranging from 40 to 500 μm, with snow density between 0.14 and 0.26 g cm^{-3}(Wang et al., 2020). The Northeast China region exhibits a larger snow particle size range (370-1550 μm) and lower snow density (0.07-0.21 g cm^{-3}). Compared with the above data, we sampled a snow particle radius of 600μm within the existing research range and used a snow density of 0.20 g cm^{-3} for study. The calculated snow specific surface area is 54 cm^2 g^{-1}.

The pseudo first order loss rate of N_2O_5 (g) on snow grain is shown in equation (R1-R2).

$$\frac{d[N_2O_5]}{dt} = -k_{het}[N_2O_5] \quad \text{(R1)}$$

$$k_{het} = \frac{1}{4}\gamma_{eff,N2O5}\bar{v} \times SA \quad \text{(R2)}$$

$$\frac{1}{\gamma_{eff,N2O5}} = \frac{1}{\Gamma_{diff}} + \frac{1}{\gamma_{N2O5,snow}} \quad \text{(R3)}$$

$$\frac{1}{\Gamma_{diff}} = \frac{8D_{SIA}}{\bar{v}(2r)} \quad \text{(R4)}$$

k_{het} is the pseudo-first-order rate coefficient, $\gamma_{eff,N2O5}$ is the effective uptake

coefficient, $\bar{\nu}$ (cm s^{-1}) is the thermal speed, and SA is the ratio of ground surface (snow grain) to volume. $\gamma_{N2O5,snow}$ and $\gamma_{eff,N2O5}$ are the reactive uptake and the effective uptake coefficient of N_2O_5 on snow grains, respectively. Γ_{diff} is a correction term for normalized gas-diffusion rate. r is the sow grain radius.

The diffusion rate in snow interstitial air (SIA) is controlled by molecular diffusion D_{SIA} (m^2 s^{-1}) (Thomas et al., 2011; Toyota et al., 2014; Wang et al., 2020). D_g is the e diffusion coefficient. λ_{air} is the mean free path. τ is the snow tortuosity ($\tau = 2$) (Wang et al., 2020).

$$D_{SIA} = \frac{D_g}{\tau} \quad \text{(R5)}$$

$$D_g = \frac{1}{3}\lambda_{air}\sqrt{8RT/(M\pi)} \quad \text{(R6)}$$

The liquid brine layer fraction (f_{brine}) in a sodium chloride solution is estimated by Eq. R7 , reflecting the enrichment of Na and Cl^- in the snow-brine layer (Cho et al., 2002). The f_{brine}, a highly concentrated salt solution, typically resides within the pores between ice crystals and should not be equated with the direct measurement of chloride ion concentration in snow meltwater samples. [Cl−](M) represents the chloride concentration in the snow brine phase, which is estimated by dividing the snow melt chloride concentrations by f_{brine}. M_{H2O} is the molecular weight of water, R is the gas constant, T_f is the freezing temperature, ΔH_f^0 is the enthalpy of fusion, and C_T is the total concentration of ions of the snowmelt sampled on the corresponding day.

$$f_{brine} = \frac{M_{H2O}RT_f}{1000\Delta H_f^0}\left(\frac{T}{T-T_f}\right)C_T \quad \text{(R7)}$$

$$\frac{1}{\gamma} = \frac{1}{\alpha} + \frac{\bar{\nu}}{4HRT\sqrt{k^I D_{aq}}} \quad \text{(R8)}$$

k^I is the pseudo-first-order rate in the brine layer. and D_{aq} is the aqueous diffusion coefficient. The $ClNO_2$ yield from snow grains ($Y_{ClNO_2,snow}$) were calculated. The parameters in k^I and $Y_{ClNO_2,snow}$ can be found in (Wang et al., 2020).

$$k^I = k_{H_2O}[H_2O] + k_{Cl^-}[Cl^-] \quad \text{(R9)}$$

$$Y_{ClNO_2,snow} = \frac{k_{Cl^-}[Cl^-]}{k_{Cl^-}[Cl^-]+k_{H_2O}[H_2O]} \quad \text{(R10)}$$

Text S2. Snow parameters observed by satellite remote sensing.

The snow parameters (depth, snow-cover, density, and albedo) were extracted from the ERA5.0 dataset to calculate monthly average spatial distribution maps for February 2024 (Fig. S4). In Northeast China, the maximum monthly average snow depth reached 0.7 m in southeastern Heilongjiang Province. Snow depth generally increased with increasing latitude across the region. Snow coverage exceeded 95% in most areas of Heilongjiang Province and parts of southeastern Jilin Province. Conversely, snow coverage was relatively low (15-30%) in western Jilin Province and the central and southwestern regions of Liaoning Province. In areas with high snow depth and coverage in Heilongjiang Province, maximum snow density reached 254 kg/m³. In other regions, snow density remained relatively constant at approximately 135 kg/m³ (Fig. S3c), consistent with the snow density range reported in the (Text S1). The reliability of the observed 0.2 g cm^{-3} (200 kg/m³) snow density was further validated using satellite data. Maximum snow albedo values reached approximately 0.73, exhibiting a correlation with snow depth snow age. This analysis presents the spatial distribution of snow parameters based on monthly averages (Figure S4b). However, it is crucial to acknowledge potential biases arising from snowmelt events, which could result in soil exposure and inaccuracies in the assessment of true snow cover conditions. The numerical range of snow variables provided by the ERA5.0 reanalysis data was utilized to verify the accuracy of snow depth, coverage, and density data obtained through field observations and laboratory physical tests in the Text S1. This validation step ensured the accuracy and effectiveness of the simulation results under regional snow conditions.

Figure captions

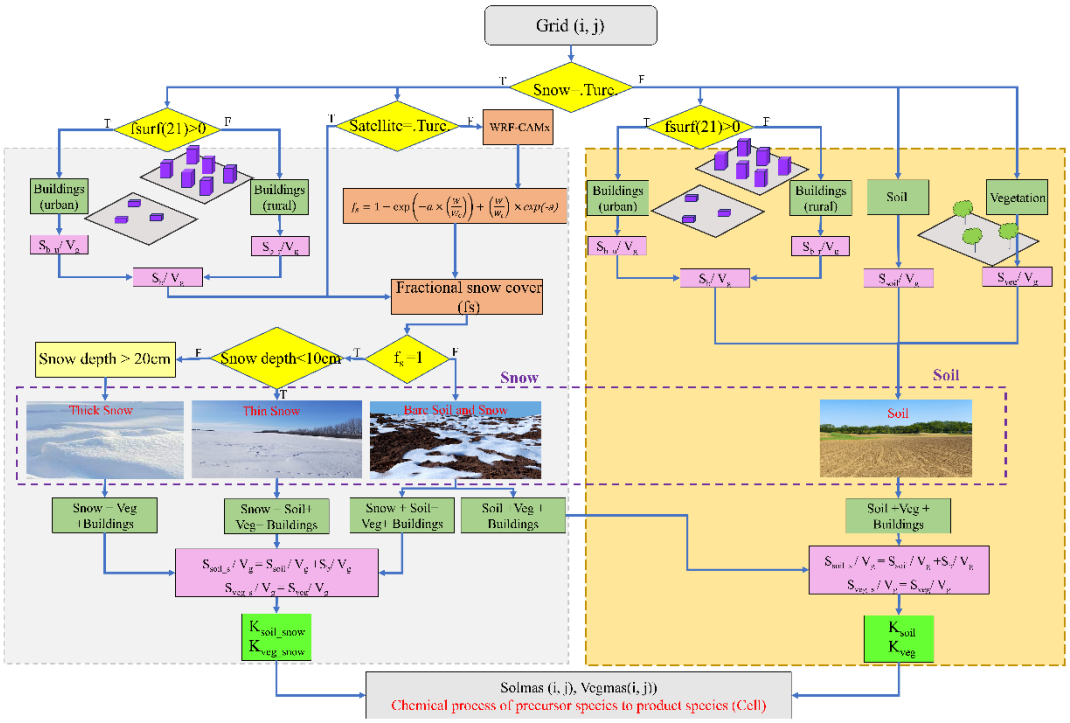

Figure S1. Characterization of S/V_g under different LU-LC.

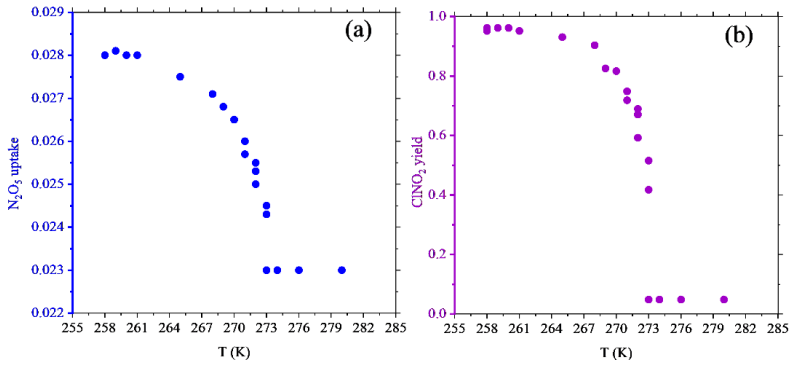

Figure S2. N_2O_5 uptake and $ClNO_2$ yield on the ground surfaces (snow, vegetation, and buildings).

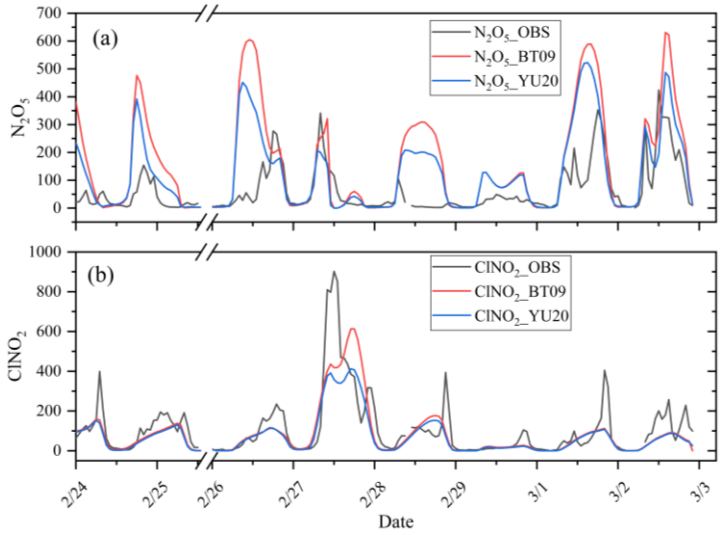

Figure S3. Comparison between simulated and observed concentrations of N_2O_5 and $ClNO_2$ under the BT09 and YU20 schemes.

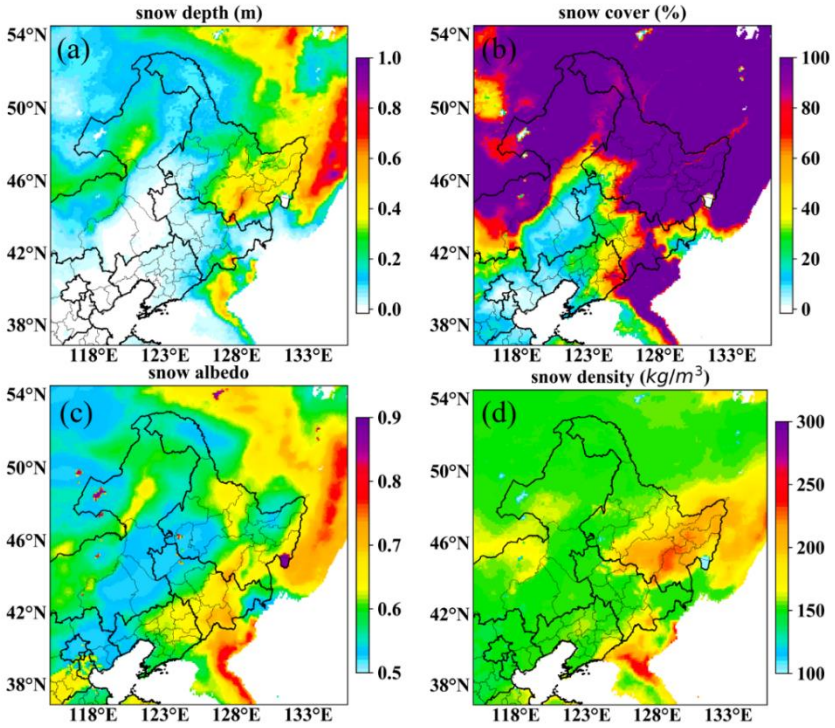

Figure S4. Monthly average spatial distribution of snow parameters (snow depth, snow cover, snow albedo and snow density).

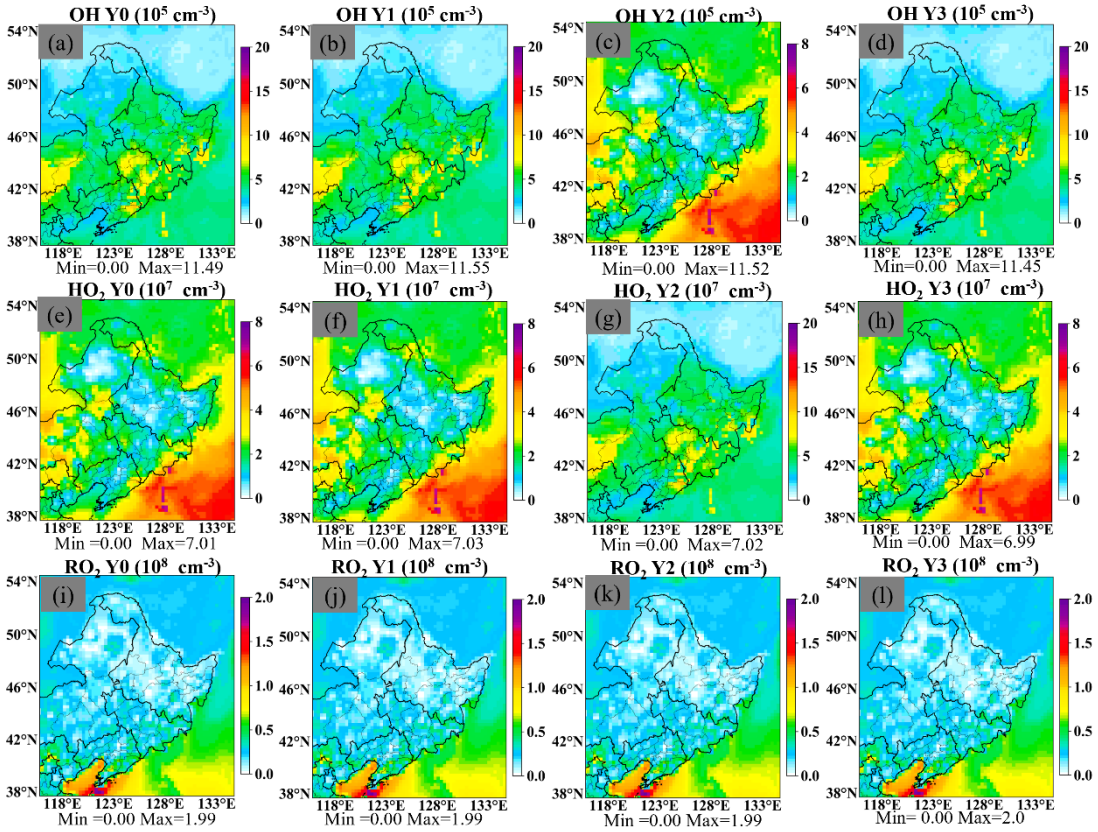

Figure S5. Spatial distribution of oxidative species (OH, HO_2, and RO_2) in different scenarios.

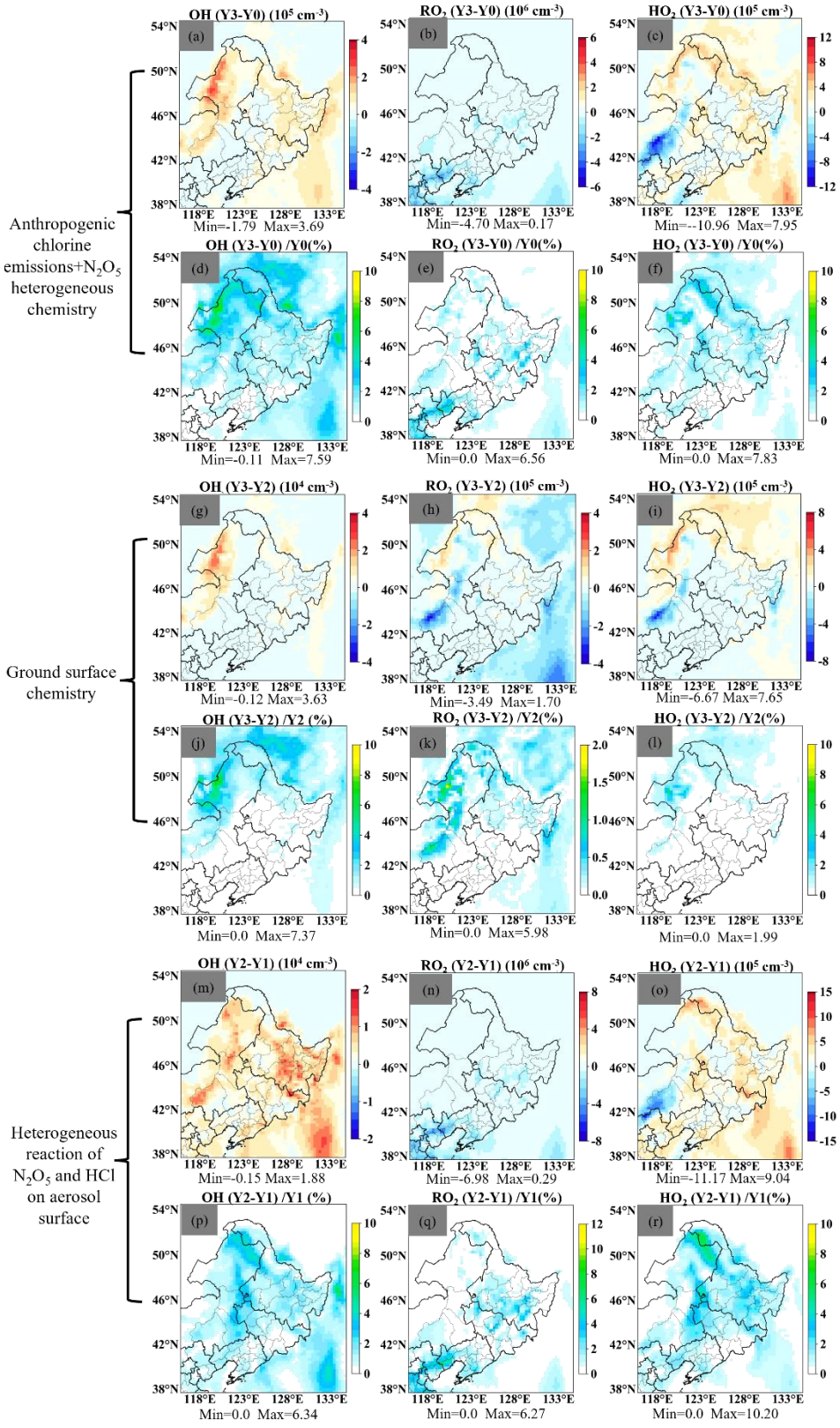

Figure S6. The quantitative contribution of different pathways of chlorine chemistry on atmospheric oxidizing capacity. The three columns of panels represent the changes

in concentrations of OH (left), RO_2 (middle), and HO_2 (right) radicals, respectively. (a–f) The bottom two rows in each group show the corresponding relative changes (%).

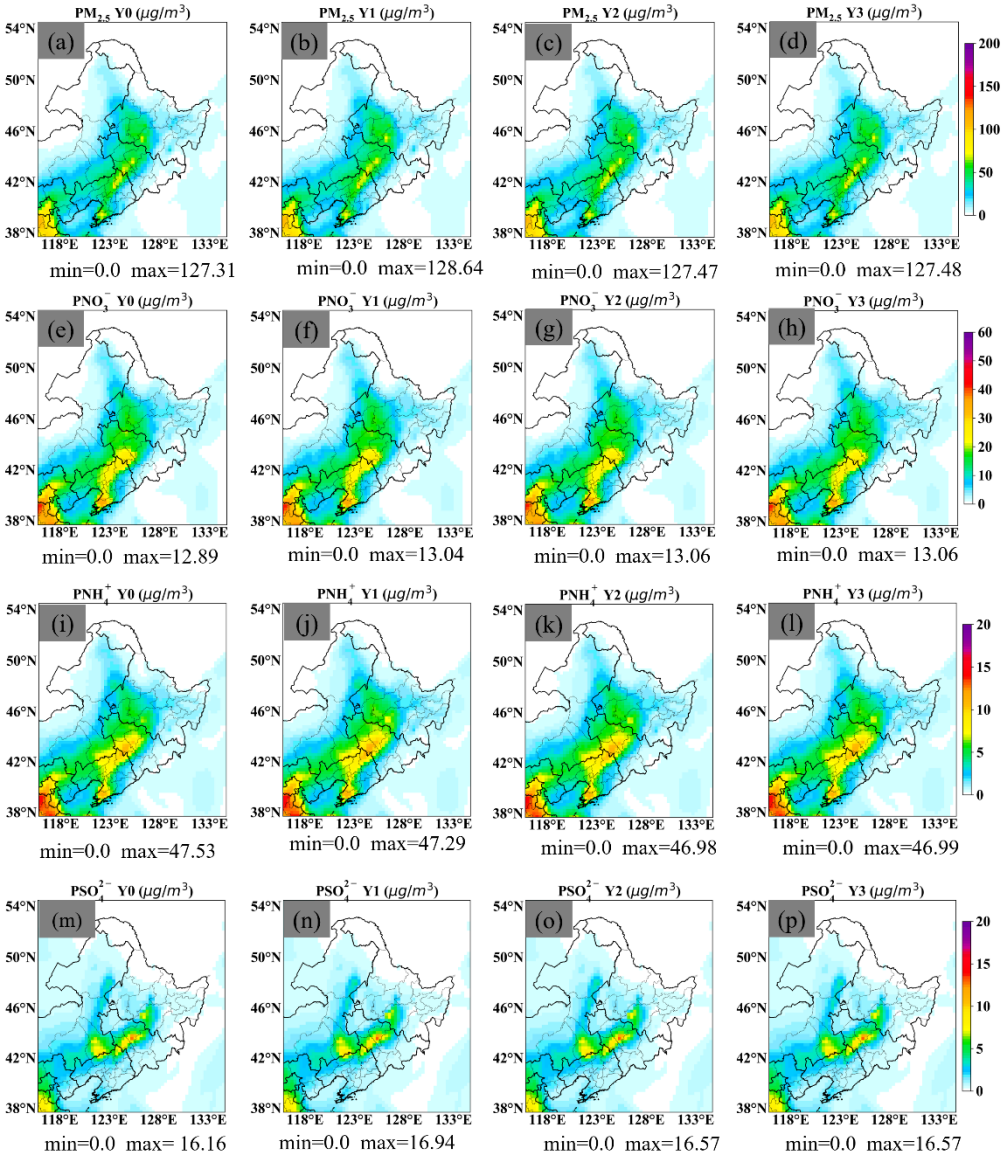

Figures S7. Spatial distribution of $PM_{2.5}$ and its component species in different scenarios.

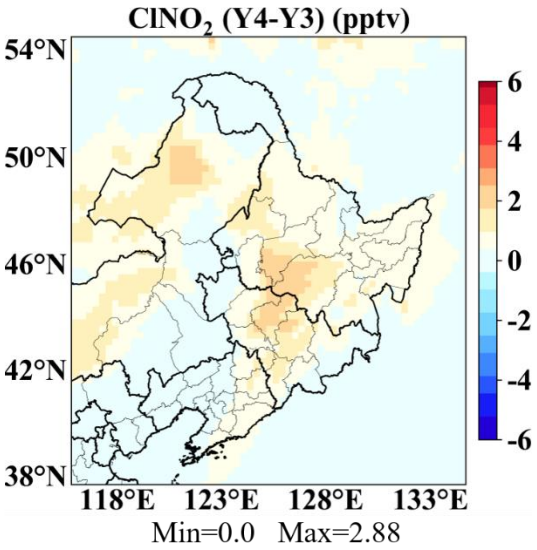

142

143 **Figure S8.** The contribution of the photolysis process of $ClNO_2$ on the ground surface

Table captions

Table S1. Chlorine emissions from the ACEIC and MEIC anthropogenic inventories used in this study (unit: Gg)

Inventory	HCl	PCl	Cl2	HOCl
ACEIC	361.34	173.72	17.55	79.45
MEIC	—	0.00	—	—

(Note: MEIC only contains PCl among chlorine species, but its emissions are set to zero; other species are not included, denoted by "—".)

Table S2. Model configurations of WRF and CAMx

WRFv3.9.1 Model Configurations		CAMxv7.10 Model Configurations	
Physics Treatment	Scheme	Model options	Scheme
Microphysics	(6) WSM6	Vertical diffusion	ACM2
Longwave radiation	(4) RRTMG	Horizontal diffusion	Explicit simultaneous 2-D solver
Shortwave radiation	(4) RRTMG	Vertical advection	PPM
Land surface model (LSM)	(2) Noah Land-Surface	Horizontal Advection	PPM
Surface layer	(1) Monin-Obukhov	Chemistry Solver	EBI
Planetary boundary layer scheme	(1) YSU	Deposition velocity	ZHANG03
Cumulus Parameterization	(5) Grell 3D	Gas-phase chemistry / Aerosol module	CB06/ CF

Table S3. Heterogeneous chemical reaction parameter scheme of N_2O_5 on aerosol surface

Parameter	CAMx Bertram (2009)	Yu (2020)
Source	Laboratory simulation	Field observations (China)
k'_{2f}	$\beta - \beta e^{(-\delta[H_2O])}$	$3.0 \times 10^4 \times [H_2O]$
k_3/k_{2b}	0.06	0.033
k_4/k_{2b}	29	3.4
k_4/k_3	483	103

Note: Determined values: $\beta = 1.15\times10^6\pm3\times10^5 s^{-1}$; $\delta = 1.3\times10^{-1}\pm5\times10^{-2}$ M^{-1} (Bertram et al., 2009).

Table S4. Comparative analysis of statistical indicators for the simulation results of N_2O_5 heterogeneous processes on atmospheric aerosol surfaces under different parameter schemes

Pollutants	Snow	Schemes	MB (pptv)	NMB (%)	RMSE (pptv)	IOA
N_2O_5	✓	BT09	114.64	1.92	201.39	0.49
	✓	YU20	69.66	1.16	139.03	0.61
$ClNO_2$	✓	BT09	-29.28	-0.28	100.66	0.81
	✓	YU20	-16.08	-0.16	99.80	0.84

References

Cho, H., Shepson, P. B., Barrie, L. A., Cowin, J. P., and Zaveri, R.: NMR investigation of the quasi-brine layer in ice/brine mixtures, The Journal of Physical Chemistry B, 106, 11226-11232, https://doi.org/10.1021/jp020449+, 2002.

Thomas, J. L., Stutz, J., Lefer, B., Huey, L. G., Toyota, K., Dibb, J. E., and von Glasow, R.: Modeling chemistry in and above snow at Summit, Greenland – Part 1: Model description and results, Atmos. Chem. Phys., 11, 4899-4914, https://doi.org/10.5194/acp-11-4899-2011, 2011.

Toyota, K., McConnell, J. C., Staebler, R. M., and Dastoor, A. P.: Air – snowpack exchange of bromine, ozone and mercury in the springtime Arctic simulated by the 1-D model PHANTAS – Part 1: In-snow bromine activation and its impact on ozone, Atmos. Chem. Phys., 14, 4101-4133, https://doi.org/10.5194/acp-14-4101-2014, 2014.

Wang, S., McNamara, S. M., Kolesar, K. R., May, N. W., Fuentes, J. D., Cook, R. D., Gunsch, M. J., Mattson, C. N., Hornbrook, R. S., Apel, E. C., and Pratt, K. A.: Urban Snowpack ClNO2 Production and Fate: A One-Dimensional Modeling Study, ACS Earth Space Chem., 4, 1140-1148, 10.1021/acsearthspacechem.0c00116, https://doi.org/10.1021/acsearthspacechem.0c00116, 2020.